Structural Engineering and Mechanics, *Vol. 51, No. 4 (2014) 685-705*
DOI: http://dx.doi.org/10.12989/sem.2014.51.4.685

Hybrid perfectly-matched-layers for transient simulation of scalar elastic waves

Alireza Pakravan[1], Jun Won Kang[*2], Craig M. Newtson[1] and Loukas F. Kallivokas[3]

[1]*Department of Civil Engineering, New Mexico State University, Las Cruces, NM 88003, USA*
[2]*Department of Civil Engineering, Hongik University, 94 Wausan-ro, Mapo-gu, Seoul 121-791, Korea*
[3]*Department of Civil, Architectural and Environmental Engineering, The University of Texas at Austin, Austin, TX 78712, USA*

(Received March 5, 2014, Revised July 15, 2014, Accepted July 20, 2014)

Abstract. This paper presents a new formulation for forward scalar wave simulations in semi-infinite media. Perfectly-Matched-Layers (PMLs) are used as a wave absorbing boundary layer to surround a finite computational domain truncated from the semi-infinite domain. In this work, a hybrid formulation was developed for the simulation of scalar wave motion in two-dimensional PML-truncated domains. In this formulation, displacements and stresses are considered as unknowns in the PML domain, while only displacements are considered to be unknowns in the interior domain. This formulation reduces computational cost compared to fully-mixed formulations. To obtain governing wave equations in the PML region, complex coordinate stretching transformation was introduced to equilibrium, constitutive, and compatibility equations in the frequency domain. Then, equations were converted back to the time-domain using the inverse Fourier transform. The resulting equations are mixed (contain both displacements and stresses), and are coupled with the displacement-only equation in the regular domain. The Newmark method was used for the time integration of the semi-discrete equations.

Keywords: perfectly-matched-layers; hybrid formulation; scalar elastic waves; PML-truncated domain; complex coordinate stretching

1. Introduction

In the simulation of wave motion, waves are frequently assumed to propagate in unbounded domains. To reduce computational cost, it is necessary to reduce the unbounded domain to a finite computational domain of interest. This domain reduction can be accomplished by a geometric truncation for the unbounded domain. Although the domain is truncated, wave motion in the truncated domain should be the same as that in the unbounded domain. A useful way to achieve this is to use Perfectly-Matched-Layers (PMLs) along a boundary to attenuate waves from the interior of the computational domain. The PML is considered to be the best absorbing boundary condition available and is widely used for various science and engineering applications such as soil-structure interaction, seismic wave propagation, non-destructive evaluation of engineering

∗Corresponding author, Assistant Professor, E-mail: jwkang@hongik.ac.kr

http://www.techno-press.org/?journal=sem&subpage=8 ISSN: 1225-4568 (Print), 1598-6217 (Online)

structures, etc. (Xu *et al*. 2013, Mahmoud and Luo 2009, Mahmoud *et al*. 2010, Madsen *et al*. 2013, Sagiyama *et al*. 2013).

The PML method was first developed by Berenger (1994) for time-domain electromagnetic waves in an unbounded domain. The formulation used splitting of electromagnetic fields into non-physical components and introduced artificial damping terms to a set of split equations within the PML. The artificial damping was later identified by Chew and Weedon (1994) as a complex coordinate transformation in the frequency-domain, by which wave attenuation is enforced. Split-field PML was then widely adopted in elastodynamics in the form of velocity-stress formulations. The split-field PML method, however, has to deal with increased number of equations involving the non-physical split variables, giving rise to additional computational cost. To circumvent this issue, various unsplit-field PML methods were developed. Among those are the Complex-Frequency-Shifted PML (CFS-PML) and C-PML, which were developed to improve the classical complex coordinate transformation that tends to produce spurious reflections if waves are highly evanescent or hit the PML with grazing incident angles (Drossaert and Giannopoulos 2007, Martin *et al*. 2008, Matzen 2011). The C-PML, however, requires specialized numerical treatment for evaluating the convolution integral. Later, the auxiliary-differential-equation PML (ADE-PML) was developed to replace the onerous evaluation of the convolution integral in the C-PML (Martin *et al*. 2010).

For time-domain elastodynamics, the split-field PML has been implemented mostly by finite-difference-time-domain (FDTD) methods, whereas the unsplit-field PML can be implemented by numerical methods based on fully unstructured meshes such as finite element methods. Basu and Chopra (2004) were among the ones who developed a displacement-based finite element formulation of the PML in the time-domain. However, their method resulted in complicated temporal integration of the semi-discrete forms. Later, Basu (2009) improved on their earlier work by using an explicit integration scheme that allowed for computational cost reduction via parallelism. However, the complexity of the formulation remained. In Kang and Kallivokas (2010), a mixed unsplit-field displacement-stress formulation in the time-domain was developed, resulting in a straightforward approach for integrating in time the resulting semi-discrete forms. However, in their approach, both displacements and stresses were considered as unknowns over both the regular and PML domains, thus adding to the computational cost.

This work improves on the earlier formulation by adopting a hybrid formulation, whereby displacements are retained as the only unknowns within the regular domain, while both stresses and displacements are unknowns within the PML domain. This leads to reduced computational cost, while retaining the second-order in time character of the semi-discrete forms. Since the number of elements in the regular domain is greater than in the PML domain, the total number of unknowns is reduced significantly by using the hybrid formulation. Creation of the semi-discrete form in the hybrid formulation relies on the fact that interface nodes between the regular and PML domains participate in the assembly of both the displacement-based finite element and the mixed form used in the PML domain.

In this paper, propagation of anti-plane (SH) waves in unbounded elastic media is simulated using: 1) truncated domains and 2) truncated domains bounded by PMLs. Wave attenuation within the PML is described via complex coordinate stretching in the frequency-domain. The corresponding time-domain equations are also discussed. A hybrid formulation is introduced for the SH-wave modeling in the PML-truncated domain, and a semi-discrete form is presented for numerical implementation. Example problems are presented that demonstrate the accuracy of the

method and the effectiveness of the PML to attenuate wave energy at the boundary.

2. SH-waves in unbounded elastic media

For a linear elastic isotropic material, the propagation of anti-plane waves is governed by the equilibrium, constitutive, and compatibility equations

$$\nabla \cdot \boldsymbol{\sigma} = \rho \frac{\partial^2 u}{\partial t^2} \tag{1}$$

$$\boldsymbol{\sigma} = 2\mu\boldsymbol{\epsilon} \tag{2}$$

$$\boldsymbol{\epsilon} = \frac{1}{2}\nabla u \tag{3}$$

where $\boldsymbol{\sigma} = [\sigma_{31}\ \sigma_{32}]^{\mathrm{T}}$ and $\boldsymbol{\epsilon} = [\epsilon_{31}\ \epsilon_{32}]^{\mathrm{T}}$ are the anti-plane shear stresses and shear strains, respectively, in Cartesian coordinates, u is the out-of-plane displacement, ρ is the mass density, and μ is the shear modulus of the medium. Indices 1, 2, and 3 indicate components along the x_1, x_2, and x_3 axes, respectively. x_3 denotes the anti-plane axis and the body force is assumed to be zero. Substituting Eqs. (2) and (3) into Eq. (1) with $v = \rho u$ and $\mu = \rho c_s^2$ yields the governing equation for the SH-wave motion in elastic media

$$\nabla \cdot (c_s^2 \nabla v) = \frac{\partial^2 v}{\partial t^2} \tag{4}$$

where v denotes normalized displacement with respect to the density and c_s denotes shear wave velocity.

3. SH-waves in the PML-truncated domain

To simulate SH-wave motion in a finite domain of interest, the original unbounded domain is truncated and surrounded by the PML with fixed outer boundary as shown in Fig. 1(a). The key idea of the wave attenuation within the PML is the complex coordinate stretching, by which the amplitude of propagating waves is exponentially diminished.

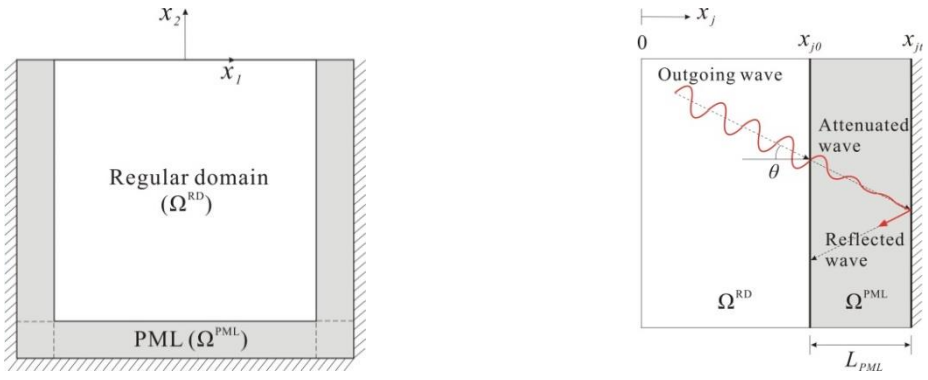

(a) PML-truncated domain (b) A PML-truncated boundary in the x_j direction

Fig. 1 PML-truncated semi-infinite domain in two-dimensions

3.1 Complex coordinate stretching

Let us assume that the regular domain occupies $0 \le x_j \le x_{j0}$ and the PML region is $x_{j0} < x_j \le x_{jt}$ with the interface between the regular domain and the PML located at x_{j0}, as shown in Fig. 1(b). As was originally suggested by Berenger (1994) and later by Chew and Weedon (1996), the complex coordinate stretching changes the original coordinate x_j (j=1, 2) to complex "stretched" coordinate $\tilde{x}_j$, defined as

$$\tilde{x}_j = \int_0^{x_j} \lambda_j(s)ds, \quad j = 1, 2 \tag{5}$$

where λ_j is a complex stretching function in the direction of coordinate x_j:

$$\lambda_j(x_j) = \alpha_j(x_j) + \frac{\beta_j(x_j)}{i\omega} \tag{6}$$

In Eq. (6), ω denotes angular frequency and i is the imaginary unit. If the coordinate stretching is introduced to propagating wave e^{-ikx_j} and evanescent wave e^{-kx_j}, with x_j replaced by $\tilde{x}_j$, the waves $e^{-ik\tilde{x}_j}$ and $e^{-k\tilde{x}_j}$ become attenuative because of the exponential decay of their amplitudes (Chew and Weedon 1996, Turkel and Yefet 1998). In such wave attenuations within the PML, α_j plays a role of the attenuation of evanescent waves, whereas β_j is responsible for the attenuation of propagating waves. Kang and Kallivokas (2010) introduced quadratic forms for α_j and β_j as

$$\alpha_j(x_j) = \begin{cases} 1, & 0 \le x_j \le x_{j0} \\ 1 + \dfrac{3b}{2L_{PML}} \log\left(\dfrac{1}{|R|}\right) \left[\dfrac{x_j - x_{j0}}{L_{PML}}\right]^2, & x_{j0} < x_j \le x_{jt} \end{cases} \tag{7}$$

$$\beta_j(x_j) = \begin{cases} 0, & 0 \le x_j \le x_{j0} \\ \dfrac{3c_{ref}}{2L_{PML}} \log\left(\dfrac{1}{|R|}\right) \left[\dfrac{x_j - x_{j0}}{L_{PML}}\right]^2, & x_{j0} < x_j \le x_{jt} \end{cases} \tag{8}$$

where $L_{PML}\,(= x_{jt} - x_{j0})$ is the length of the PML in the x_j direction and $|R|$ is a user-tunable reflection coefficient that controls the amount of reflection from the fixed PML end ($x_j = x_{jt}$). In Eq. (7), b is a characteristic length of the domain (e.g., element size), while in Eq. (8), c_{ref} is a reference shear wave velocity in the domain.

Differentiating Eq. (8) with respect to x_j leads to the following differential operator

$$\frac{d}{d\tilde{x}_j} = \frac{1}{\lambda_j(x_j)} \frac{d}{dx_j} \tag{9}$$

In applying the coordinate stretching to governing differential equations, one can replace the derivative $\partial/\partial x_j$, $(j = 1, 2)$ in the equations with $\partial/\partial \tilde{x}_j$, which, in turn, can be rewritten in terms of the original coordinate by Eq. (9).

3.2 Frequency-domain equations

The equilibrium, constitutive, and compatibility equations in the frequency-domain for the SH wave motion can be obtained by the Fourier transform of Eqs. (1)-(3)

$$\nabla \cdot \hat{\boldsymbol{\sigma}} = -\omega^2 \rho \hat{u} \tag{10}$$

$$\hat{\boldsymbol{\sigma}} = 2\mu \hat{\boldsymbol{\epsilon}} \tag{11}$$

$$\hat{\boldsymbol{\epsilon}} = \frac{1}{2} \nabla \hat{u} \tag{12}$$

where a caret (^) denotes the Fourier transform of the subtended function. The complex coordinate stretching is applied first to the equilibrium equation (10) by replacing x_1 and x_2 with the stretched coordinates $\tilde{x}_1$ and $\tilde{x}_2$, respectively. Then, using unabridged notation, Eq. (10) becomes

$$\frac{\partial \hat{\sigma}_{31}}{\partial \tilde{x}_1} + \frac{\partial \hat{\sigma}_{32}}{\partial \tilde{x}_2} = -\omega^2 \rho \hat{u} \tag{13}$$

Making use of Eq. (9), Eq. (13) can be rewritten in terms of the original coordinates as

$$\frac{1}{\lambda_1} \frac{\partial \hat{\sigma}_{31}}{\partial x_1} + \frac{1}{\lambda_2} \frac{\partial \hat{\sigma}_{32}}{\partial x_2} = -\omega^2 \rho \hat{u} \tag{14}$$

Multiplying both sides of Eq. (14) by $\lambda_1 \lambda_2$ and recalling that λ_1 depends on x_1 and λ_2 depends on x_2, Eq. (14) can be modified as

$$\nabla \cdot \left(\tilde{\boldsymbol{\Lambda}} \hat{\boldsymbol{\sigma}} \right) = -\omega^2 \lambda_1 \lambda_2 \hat{u} \tag{15}$$

in which the stretching tensor $\tilde{\boldsymbol{\Lambda}}$ is defined as (identical to the definition by Basu and Chopra 2004)

$$\tilde{\boldsymbol{\Lambda}} = \begin{bmatrix} \lambda_2 & 0 \\ 0 & \lambda_1 \end{bmatrix} = \begin{bmatrix} \alpha_2 & 0 \\ 0 & \alpha_1 \end{bmatrix} + \frac{1}{i\omega} \begin{bmatrix} \beta_2 & 0 \\ 0 & \beta_1 \end{bmatrix} = \tilde{\boldsymbol{\Lambda}}^e + \frac{1}{i\omega} \tilde{\boldsymbol{\Lambda}}^p \tag{16}$$

and the superscripts *e* and *p* represent the evanescent and propagating wave attenuations, respectively. Substituting Eqs. (16) and (6) into Eq. (15) and rearranging terms results in

$$\nabla \cdot \left[\tilde{\boldsymbol{\Lambda}}^e \hat{\boldsymbol{\sigma}} + \frac{1}{i\omega} \tilde{\boldsymbol{\Lambda}}^p \hat{\boldsymbol{\sigma}} \right] = \rho [-\omega^2 a \hat{u} + i\omega b \hat{u} + c \hat{u}] \tag{17}$$

where

$$a = \alpha_1 \alpha_2 \,, \quad b = \alpha_1 \beta_2 + \alpha_2 \beta_1 \,, \quad c = \beta_1 \beta_2 \tag{18}$$

Next, the coordinate stretching is applied to the compatibility equation (12) to yield

$$\hat{\boldsymbol{\epsilon}} = \frac{1}{2} \begin{bmatrix} \frac{1}{\lambda_1} & 0 \\ 0 & \frac{1}{\lambda_2} \end{bmatrix} \begin{bmatrix} \frac{\partial \hat{u}}{\partial x_1} \\ \frac{\partial \hat{u}}{\partial x_2} \end{bmatrix} = \frac{1}{2} \boldsymbol{\Lambda} \nabla \hat{u} \tag{19}$$

where the stretching tensor $\boldsymbol{\Lambda}$ is defined as

$$\boldsymbol{\Lambda} = \begin{bmatrix} \dfrac{1}{\lambda_1} & 0 \\ 0 & \dfrac{1}{\lambda_2} \end{bmatrix} \tag{20}$$

Pre-multiplying both sides of Eq. (19) by $i\omega\boldsymbol{\Lambda}^{-1}$ results in

$$i\omega\boldsymbol{\Lambda}^{-1}\hat{\boldsymbol{\epsilon}} = \frac{1}{2}(i\omega)\nabla\hat{u} \tag{21}$$

where

$$\boldsymbol{\Lambda}^{-1} = \begin{bmatrix} \lambda_1 & 0 \\ 0 & \lambda_2 \end{bmatrix} = \begin{bmatrix} \alpha_1 & 0 \\ 0 & \alpha_2 \end{bmatrix} + \frac{1}{i\omega}\begin{bmatrix} \beta_1 & 0 \\ 0 & \beta_2 \end{bmatrix} = \boldsymbol{\Lambda}^e + \frac{1}{i\omega}\boldsymbol{\Lambda}^p \tag{22}$$

Substituting Eq. (22) into Eq. (21) yields

$$i\omega\boldsymbol{\Lambda}^e\hat{\boldsymbol{\epsilon}} + \boldsymbol{\Lambda}^p\hat{\boldsymbol{\epsilon}} = \frac{1}{2}(i\omega)\nabla\hat{u} \tag{23}$$

Eqs. (17), (11), and (23) are frequency-domain equations of equilibrium, constitutive relationship, and compatibility in the coordinate-stretched PML domain. Notice that, within the regular domain, $\widetilde{\boldsymbol{\Lambda}}^e = \boldsymbol{\Lambda}^e = \mathbf{I}$, $\widetilde{\boldsymbol{\Lambda}}^p = \boldsymbol{\Lambda}^p = \mathbf{0}$, $a = 1$, $b = 0$, and $c = 0$, and Eqs. (17), (11), and (23) reduce to Eqs. (10)-(12).

3.3 Time-domain equations

Applying the inverse Fourier transform to frequency-domain Eqs. (17), (11), and (23), written for both the regular and PML domains, yields the corresponding equations in the time-domain

$$\nabla\cdot\left[\widetilde{\boldsymbol{\Lambda}}^e\boldsymbol{\sigma} + \widetilde{\boldsymbol{\Lambda}}^p\int_0^t \boldsymbol{\sigma}\, d\tau\right] = \rho[a\ddot{u} + b\dot{u} + cu] \tag{24}$$

$$\boldsymbol{\sigma} = 2\mu\boldsymbol{\epsilon} \tag{25}$$

$$\boldsymbol{\Lambda}^e\dot{\boldsymbol{\epsilon}} + \boldsymbol{\Lambda}^p\boldsymbol{\epsilon} = \frac{1}{2}\nabla\dot{u} \tag{26}$$

In Eq. (24), the stress integration term represents stress memory or history, and can be defined by introducing an auxiliary variable $\mathbf{s}(\mathbf{x},t)$ as

$$\mathbf{s}(\mathbf{x},t) = \int_0^t \boldsymbol{\sigma}(\mathbf{x},t)\, d\tau\ , \quad \mathbf{s} = [s_1\ \ s_2]^T \tag{27}$$

such that

$$\dot{\mathbf{s}}(\mathbf{x},t) = \boldsymbol{\sigma}(\mathbf{x},t)\ , \quad \ddot{\mathbf{s}}(\mathbf{x},t) = \dot{\boldsymbol{\sigma}}(\mathbf{x},t) \tag{28}$$

The stretched time-domain constitutive and compatibility equations (25) and (26) can be combined together to yield

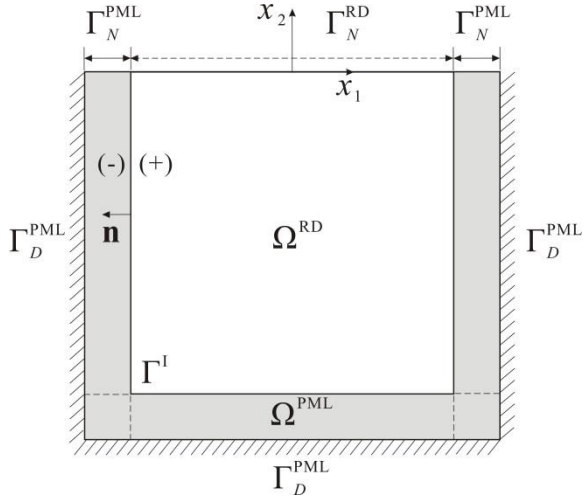

Fig. 2 Schematic of a two-dimensional PML-truncated domain for a hybrid SH-wave formulation

$$\boldsymbol{\Lambda}^e\dot{\boldsymbol{\sigma}} + \boldsymbol{\Lambda}^p\boldsymbol{\sigma} = \mu\nabla\dot{u} \tag{29}$$

By substituting Eqs. (27) and (28) into Eqs. (24) and (29), while again setting $v = \rho u$, a displacement (v)-stress memory ($\mathbf{s}$) mixed form of the equations governing the propagation of SH waves in the PML-truncated domain can be obtained as the following

$$\nabla \cdot \left[\widetilde{\boldsymbol{\Lambda}}^e\dot{\mathbf{s}} + \widetilde{\boldsymbol{\Lambda}}^p\mathbf{s}\right] = a\ddot{v} + b\dot{v} + cv \tag{30}$$

$$\boldsymbol{\Lambda}^e\ddot{\mathbf{s}} + \boldsymbol{\Lambda}^p\dot{\mathbf{s}} = c_s^2\nabla\dot{v} \tag{31}$$

4. Hybrid SH-wave modeling

To obtain approximate solutions to Eqs. (30) and (31), a mixed finite element method can be employed, where both displacement (v) and stress memories ($\mathbf{s}$) are treated as independent unknowns throughout the entire computational domain (Frasca *et al*. 1988, Brezzi and Bathe 1990, Bécache *et al*. 2002). The mixed method is relatively straightforward and economical compared to conventional split-field PML formulations (Chew and Liu 1996, Hastings *et al*. 1996, Komatitsch and Tromp 2003), but still requires additional unknowns (stress memories) in the regular domain as opposed to a displacement-based finite element method.

In this work, a hybrid approach is presented to further reduce the computational cost of the fully-mixed method in terms of the number of degrees-of-freedom. Specifically, a single-field formulation (displacement only) is used for the regular domain problem, and it is coupled with the mixed formulation for the PML. In other words, Eq. (4) is used as the governing wave equation in the regular domain (Ω^{RD}), whereas Eqs. (30) and (31) are used for governing equations in the PML (Ω^{PML}), with the two domains coupled by continuity conditions of displacement and stresses. Therefore, the SH-wave motion in the two-dimensional PML-truncated domain (Fig. 2) is governed by the following system of equations

$$\nabla \cdot (c_s^2 \nabla v) = \frac{\partial^2 v}{\partial t^2} \qquad \text{in } \Omega^{RD} \times (0,T] \tag{32}$$

$$\nabla \cdot \left[\widetilde{\boldsymbol{\Lambda}}^e \dot{\mathbf{s}} + \widetilde{\boldsymbol{\Lambda}}^p \mathbf{s}\right] = a\ddot{v} + b\dot{v} + cv \qquad \text{in } \Omega^{PML} \times (0,T] \tag{33}$$

$$\boldsymbol{\Lambda}^e \ddot{\mathbf{s}} + \boldsymbol{\Lambda}^p \dot{\mathbf{s}} = c_s^2 \nabla \dot{v} \qquad \text{in } \Omega^{PML} \times (0,T] \tag{34}$$

subject to the following initial conditions

$$v(\mathbf{x},0) = 0, \quad \dot{v}(\mathbf{x},0) = 0, \qquad \text{in } \Omega \tag{35}$$

$$\mathbf{s}(\mathbf{x},0) = 0, \quad \dot{\mathbf{s}}(\mathbf{x},0) = 0, \qquad \text{in } \Omega \tag{36}$$

and the following boundary and interface continuity conditions

$$c_s^2 \nabla v \cdot \mathbf{n} = p(\mathbf{x},t) \qquad \text{on } \Gamma_N^{RD} \times (0,T] \tag{37}$$

$$\left(\widetilde{\boldsymbol{\Lambda}}^e \dot{\mathbf{s}} + \widetilde{\boldsymbol{\Lambda}}^p \mathbf{s}\right) \cdot \mathbf{n} = 0 \qquad \text{on } \Gamma_N^{PML} \times (0,T] \tag{38}$$

$$v = 0 \qquad \text{on } \Gamma_D^{PML} \times (0,T] \tag{39}$$

$$v^+ = v^- \qquad \text{on } \Gamma^I \times (0,T] \tag{40}$$

$$c_s^2 \nabla v \cdot \mathbf{n} = -\left(\widetilde{\boldsymbol{\Lambda}}^e \dot{\mathbf{s}} + \widetilde{\boldsymbol{\Lambda}}^p \mathbf{s}\right) \cdot \mathbf{n} \qquad \text{on } \Gamma^I \times (0,T] \tag{41}$$

where $p(\mathbf{x},t)$ denotes prescribed tractions on Γ_N^{RD}. In the above system, Eqs. (40) and (41) are continuity conditions of the displacement and stresses at the interface (Γ^I) between the regular domain and the PML.

The Galerkin approach is used to obtain the weak form corresponding to the strong form (32)-(41). Specifically, Eqs. (32) and (33) are multiplied by test functions $w_1(\mathbf{x})$ and $w_2(\mathbf{x})$, and then integrated over Ω^{RD} and Ω^{PML}, respectively. Similarly, an inner product is taken over the vector Eq. (34) with a test function vector $\mathbf{q}(\mathbf{x})$, and the resulting equation is integrated over Ω^{PML}. In this process, integration by parts is applied only to Eqs. (32) and (33). Adding the individual weak forms for Eqs. (32) and (33) results in the weak form of the entire system as: find $v \in H^1(\Omega) \times (0,T]$ satisfying $v|_{\Gamma_D^{PML}} = 0$, and $\mathbf{s} \in \mathbf{L}^2(\Omega) \times (0,T]$, such that the following equations are satisfied for all $w_1 \in H^1(\Omega)$, $w_2 \in H^1(\Omega)$ satisfying $w_2|_{\Gamma_D^{PML}} = 0$, and $\mathbf{q}(\mathbf{x}) \in \mathbf{L}^2(\Omega)$

$$\begin{aligned}\int_{\Omega^{RD}} w_1 \ddot{v}\, d\Omega + \int_{\Omega^{PML}} w_2(a\ddot{v} + b\dot{v} + cv)d\Omega + \int_{\Omega^{RD}} \nabla w_1 \cdot (c_s^2 \nabla v)d\Omega \\ + \int_{\Omega^{PML}} \nabla w_2 \cdot \left(\widetilde{\boldsymbol{\Lambda}}^e \dot{\mathbf{s}} + \widetilde{\boldsymbol{\Lambda}}^p \mathbf{s}\right) d\Omega = \int_{\Gamma_N^{RD}} w_1 p(\mathbf{x},t) d\Gamma\end{aligned} \tag{42}$$

$$\int_{\Omega^{PML}} \mathbf{q} \cdot (\boldsymbol{\Lambda}^e \ddot{\mathbf{s}} + \boldsymbol{\Lambda}^p \dot{\mathbf{s}}) d\Omega = \int_{\Omega^{PML}} \mathbf{q} \cdot (c_s^2 \nabla \dot{v}) d\Omega \tag{43}$$

In obtaining Eq. (42), continuity conditions (40) and (41) were imposed with the test function

requirement $w_1 = w_2$ along the interface. The function spaces used for trial and test functions are

$$H^1(\Omega) = \left\{ h(\mathbf{x}) : \int_\Omega h^2 + \left(\frac{dh}{dx}\right)^2 dx < \infty \right\} \tag{44}$$

$$\mathbf{L}^2(\Omega) = \left\{ \mathbf{h}(\mathbf{x}) = [h_1(\mathbf{x}) \;\; h_2(\mathbf{x}) \cdots h_N(\mathbf{x})]^T : \int_\Omega h_i^2 dx < \infty, \;\; i = 1,2,\cdots,N \right\} \tag{45}$$

For the mixed finite element implementation of the variational forms (42) and (43), displacement $v(\mathbf{x},t)$ and stress memories $\mathbf{s}(\mathbf{x},t)$ can be independently approximated using basis functions $\phi_i(\mathbf{x}) \in H^1(\Omega)$ and $\psi_i(\mathbf{x}) \in L^2(\Omega)$, respectively, within the PML. On the other hand, $v(\mathbf{x},t)$ has only to be approximated within the regular domain. The trial functions $v_h \in H^1(\Omega) \times (0,T]$ and $\mathbf{s}_h \in \mathbf{L}^2(\Omega) \times (0,T]$ are spatially discretized as

$$v(\mathbf{x},t) \cong v_h(\mathbf{x},t) = \boldsymbol{\phi}^T(\mathbf{x})\mathbf{v}(t) \tag{46}$$

$$\mathbf{s}(\mathbf{x},t) \cong \mathbf{s}_h(\mathbf{x},t) = \begin{bmatrix} \boldsymbol{\psi}^T(\mathbf{x})\mathbf{s}_1(t) \\ \boldsymbol{\psi}^T(\mathbf{x})\mathbf{s}_2(t) \end{bmatrix} \tag{47}$$

where $\boldsymbol{\phi}$ and $\boldsymbol{\psi}$ are column vectors of the basis functions associated with nodal displacements ($\mathbf{v} = \rho\mathbf{u}$) and nodal stress memories ($\mathbf{s}_1$, $\mathbf{s}_2$), respectively. The test functions w_1, w_2, and $\mathbf{q}$ are similarly approximated by the same basis functions as

$$w_1(\mathbf{x}) \cong w_{1h}(\mathbf{x}) = \mathbf{w}_1^T\boldsymbol{\phi}(\mathbf{x}) \tag{48}$$

$$w_2(\mathbf{x}) \cong w_{2h}(\mathbf{x}) = \mathbf{w}_2^T\boldsymbol{\phi}(\mathbf{x}) \tag{49}$$

$$\mathbf{q}(\mathbf{x}) \cong \mathbf{q}_h(\mathbf{x}) = \begin{bmatrix} \mathbf{q}_1^T\boldsymbol{\psi}(\mathbf{x}) \\ \mathbf{q}_2^T\boldsymbol{\psi}(\mathbf{x}) \end{bmatrix} \tag{50}$$

where $\mathbf{w}_1$, $\mathbf{w}_2$, $\mathbf{q}_1$, and $\mathbf{q}_2$ are vectors of nodal test function values. Introducing Eqs. (46)-(50) into Eqs. (42) and (43) yields the following semi-discrete form

$$\mathbf{M}\ddot{\mathbf{U}} + \mathbf{C}\dot{\mathbf{U}} + \mathbf{K}\mathbf{U} = \mathbf{F} \tag{51}$$

where the system matrices $\mathbf{M}$, $\mathbf{C}$, $\mathbf{K}$ and the vectors $\mathbf{U}$ and $\mathbf{F}$ are constructed as

$$\mathbf{M} = \begin{bmatrix} \mathbf{M}^{11} & \mathbf{0} & \mathbf{0} & \mathbf{0} \\ \mathbf{0} & \mathbf{M}^{22} & \mathbf{0} & \mathbf{0} \\ \mathbf{0} & \mathbf{0} & \mathbf{M}^{33} & \mathbf{0} \\ \mathbf{0} & \mathbf{0} & \mathbf{0} & \mathbf{M}^{44} \end{bmatrix}, \quad \mathbf{C} = \begin{bmatrix} \mathbf{0} & \mathbf{0} & \mathbf{0} & \mathbf{0} \\ \mathbf{0} & \mathbf{C}^{22} & \mathbf{C}^{23} & \mathbf{C}^{24} \\ \mathbf{0} & \mathbf{C}^{32} & \mathbf{C}^{33} & \mathbf{0} \\ \mathbf{0} & \mathbf{C}^{42} & \mathbf{0} & \mathbf{C}^{44} \end{bmatrix} \tag{52}$$

$$\mathbf{K} = \begin{bmatrix} \mathbf{K}^{11} & \mathbf{0} & \mathbf{0} & \mathbf{0} \\ \mathbf{0} & \mathbf{K}^{22} & \mathbf{K}^{23} & \mathbf{K}^{24} \\ \mathbf{0} & \mathbf{0} & \mathbf{0} & \mathbf{0} \\ \mathbf{0} & \mathbf{0} & \mathbf{0} & \mathbf{0} \end{bmatrix} \tag{53}$$

$$\mathbf{U} = \begin{bmatrix} \mathbf{v}^r & \mathbf{v}^p & \mathbf{s}_1^p & \mathbf{s}_2^p \end{bmatrix}^T, \quad \mathbf{F} = [\mathbf{f}^r \quad \mathbf{0} \quad \mathbf{0} \quad \mathbf{0}]^T \tag{54}$$

In the above vectors, indices r and p indicate the regular and the PML domains, respectively. The component of various sub-matrices and vectors in Eqs. (52)-(54) can be constructed as

$$\mathbf{M}_{ij}^{11} = \int_{\Omega^{RD}} \phi_i \phi_j d\Omega\,, \qquad \mathbf{M}_{ij}^{22} = \int_{\Omega^{PML}} a\phi_i \phi_j d\Omega\,, \tag{55}$$

$$\mathbf{M}_{ij}^{33} = \int_{\Omega^{PML}} \alpha_1 \psi_i \psi_j d\Omega\,, \qquad \mathbf{M}_{ij}^{44} = \int_{\Omega^{PML}} \alpha_2 \psi_i \psi_j d\Omega\,, \tag{56}$$

$$\mathbf{C}_{ij}^{22} = \int_{\Omega^{PML}} b\phi_i \phi_j d\Omega\,, \qquad \mathbf{C}_{ij}^{23} = \int_{\Omega^{PML}} \alpha_2 \frac{\partial \phi_i}{\partial x_1} \psi_j d\Omega\,, \qquad \mathbf{C}_{ij}^{24} = \int_{\Omega^{PML}} \alpha_1 \frac{\partial \phi_i}{\partial x_2} \psi_j d\Omega\,, \tag{57}$$

$$\mathbf{C}_{ij}^{32} = -\int_{\Omega^{PML}} c_s^2 \psi_i \frac{\partial \phi_j}{\partial x_1} d\Omega\,, \qquad \mathbf{C}_{ij}^{33} = \int_{\Omega^{PML}} \beta_1 \psi_i \psi_j d\Omega\,, \tag{58}$$

$$\mathbf{C}_{ij}^{42} = -\int_{\Omega^{PML}} c_s^2 \psi_i \frac{\partial \phi_j}{\partial x_2} d\Omega\,, \qquad \mathbf{C}_{ij}^{44} = \int_{\Omega^{PML}} \beta_2 \psi_i \psi_j d\Omega\,, \tag{59}$$

$$\mathbf{K}_{ij}^{11} = \int_{\Omega^{RD}} c_s^2 \left(\frac{\partial \phi_i}{\partial x_1} \frac{\partial \phi_j}{\partial x_1} + \frac{\partial \phi_i}{\partial x_2} \frac{\partial \phi_j}{\partial x_2} \right) d\Omega\,, \qquad \mathbf{K}_{ij}^{22} = \int_{\Omega^{PML}} c\phi_i \phi_j d\Omega\,, \tag{60}$$

$$\mathbf{K}_{ij}^{23} = \int_{\Omega^{PML}} \beta_2 \frac{\partial \phi_i}{\partial x_1} \psi_j d\Omega\,, \qquad \mathbf{K}_{ij}^{24} = \int_{\Omega^{PML}} \beta_1 \frac{\partial \phi_i}{\partial x_2} \psi_j d\Omega\,, \tag{61}$$

$$i, j = 1, \cdots, N_r \text{ for } \mathbf{M}_{ij}^{11} \text{ and } \mathbf{K}_{ij}^{11}$$

$$i, j = 1, \cdots, N_p \text{ for the other sub-matrices}$$

$$\mathbf{f}_i^r = \int_{\Gamma_N^{RD}} \phi_i p(\mathbf{x}, t) d\Omega\,, \quad i = 1, \cdots, N_r \tag{62}$$

where N_r and N_p denote total numbers of nodes within the regular and the PML domains, respectively. In the above expressions, ϕ_k and ψ_k $(k = i, j)$ are classical Lagrange basis functions used for the approximation of displacement and stress memories, respectively. It is noted that the sub-matrices $\mathbf{M}^{11}$ and $\mathbf{K}^{11}$ are constructed from regular domain elements, whereas the other sub-matrices are constructed from PML domain elements.

The hybrid formulation for the simulation of SH-waves in the PML-truncated domain is computationally more economical compared to a fully-mixed formulation, since, in the hybrid case, only displacement is taken as a variable within the regular domain as opposed to the fully-mixed case where both displacement and stresses should be taken as independent variables. The semi-discrete form (51) can be integrated with respect to time using a standard Newmark-β method.

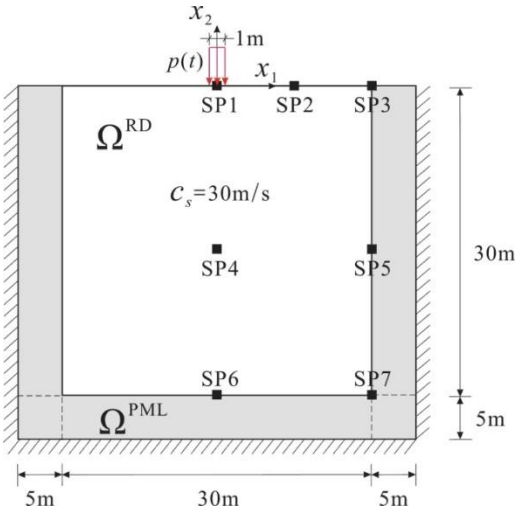

Fig. 3 A homogeneous PML-truncated two-dimensional domain subjected to a shear stress load $p(t)$ on its surface

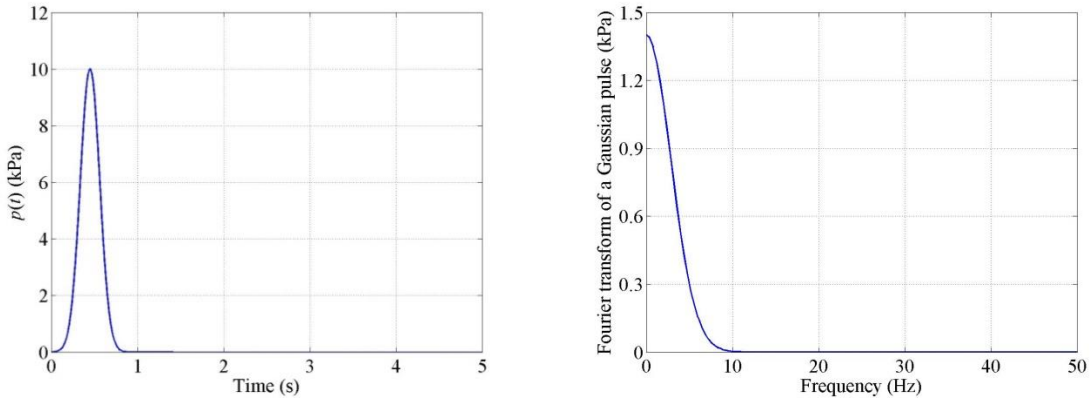

(a) (b)

Fig. 4 (a) Excitation time signal $p(t)$ and (b) its Fourier spectrum

5. Numerical examples

5.1 Homogeneous media

Consider first a 30m×30m truncated half-plane (computational domain) surrounded on its sides and bottom by a 5m PML as shown in Fig. 3. The domain is homogeneous with density $\rho = 2000\ \mathrm{kg/m^3}$ and shear wave velocity $c_s = 30\ \mathrm{m/s}$. Both the regular and the PML domains were discretized by quadratic elements with an element size of 0.5m. The discretization resulted in 10 elements within each PML layer. The reflection coefficient $|R|$ in Eqs. (7)-(8) was taken as 10^{-4} in the PML domain. To excite the domain, a Gaussian pulse-type stress load $\sigma_{32} = p(t)$ was applied over a surface region with coordinates of $x_2 = 0$ and $-0.5\mathrm{m} \le x_1 \le 0.5\mathrm{m}$. Fig. 4

shows the time history and the frequency spectrum of the excitation. As can be seen in the frequency spectrum, the maximum frequency is roughly 9Hz, and accordingly, the minimum period of superimposed harmonic waves in the time signal is about 0.111s. The time step Δt was determined such that the minimum period could be divided by at least 15 discrete time points. In this work, a time step of 0.002 s was used in all numerical simulations. The time histories of the anti-plane displacement were collected at seven sampling points (SP*i*, *i*=1, 2,⋯, 7) as described in Fig. 3.

To verify the accuracy of solutions obtained from the hybrid formulation, response time histories at the sampling points were compared with the displacement-based finite element solution of an enlarged domain with fixed boundaries. Fig. 5 compares the displacement responses of the PML-truncated and enlarged domains for 5 seconds at various sampling points within the computational domain. It is seen that the PML effectively absorbed the waves without reflections and that the responses for the enlarged domain and the PML-truncated domain do not differ noticeably. Fig. 6 depicts the responses for 50 seconds that correspond to 25,000 time steps, which demonstrates the numerical stability of the hybrid formulation for SH waves.

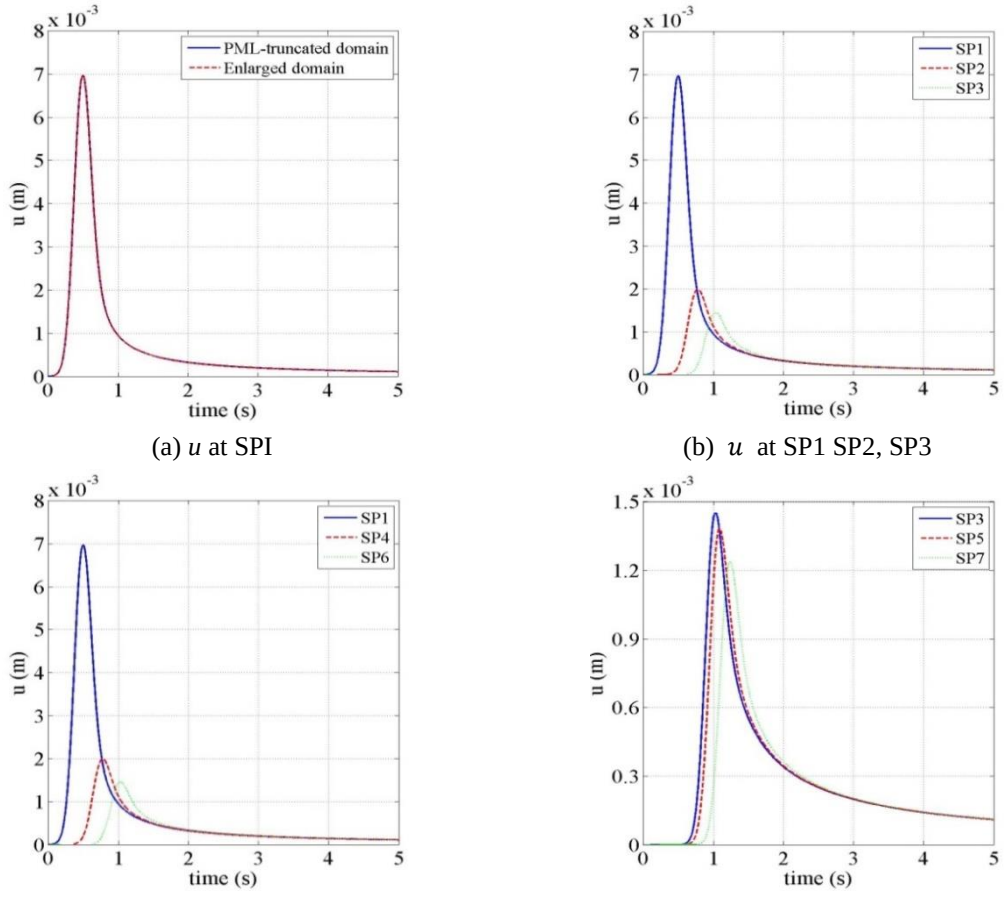

(a) u at SPI

(b) u at SP1 SP2, SP3

(c) u at SP1 SP4, SP6

(d) u at SP3 SP5, SP7

Fig. 5 Displacement time histories at various sampling points

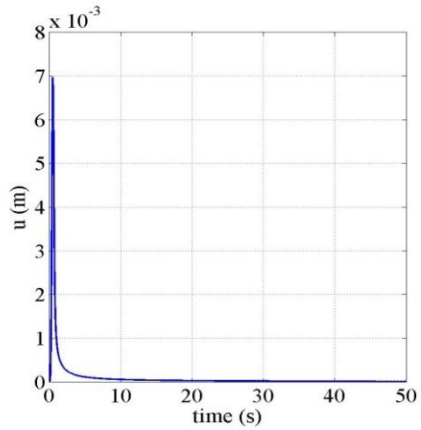

Fig. 6 Long term stability of solutions from the hybrid formulation

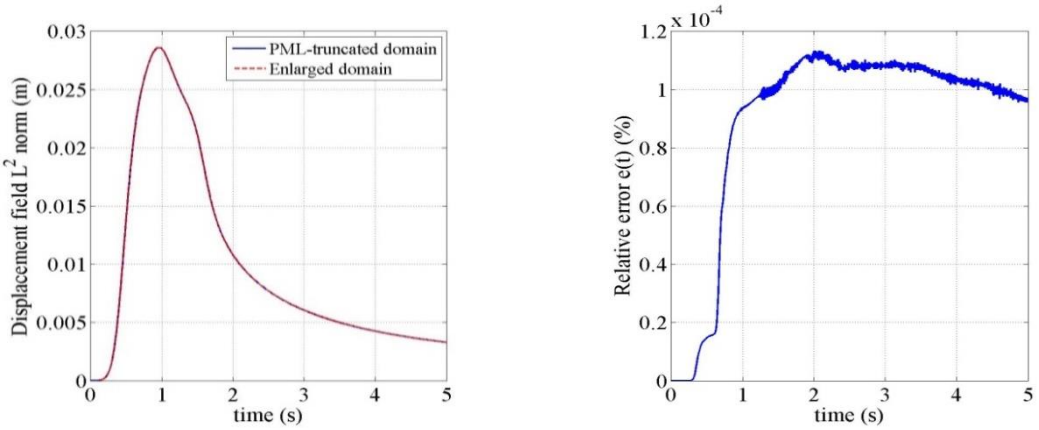

(a) Displacement field L^2 norm $D(t, \Omega^{RD})$ (b) Relative error $e(t)$

Fig. 7 Error metrics for the homogeneous domain excited by a surface Gaussian pulse $p(t)$

To investigate the accuracy of solutions of the hybrid formulation, two error metrics are defined. First, the L^2 norm of the displacement over a domain Ω is introduced as

$$D(t,\Omega) = \int_{\Omega} u^2(\mathbf{x},t)d\Omega \tag{63}$$

Next, the time-dependent relative error in terms of L^2 norms, normalized with respect to the peak value of the L^2 norm within the enlarged domain is defined as

$$e(t) = \frac{\left\{\int_{\Omega^{RD}}[u(\mathbf{x},t) - u_{LD}(\mathbf{x},t)]^2 d\Omega^{RD}\right\}^{\frac{1}{2}}}{\max_{\mathrm{t}} D(t,\Omega^{LD})} \times 100 \tag{64}$$

Using the calculated displacements in the PML-truncated and enlarged domains, $D(t, \Omega)$ is computed for the two cases but only in the regular region. The two L^2 norms are compared in Fig. 7(a),

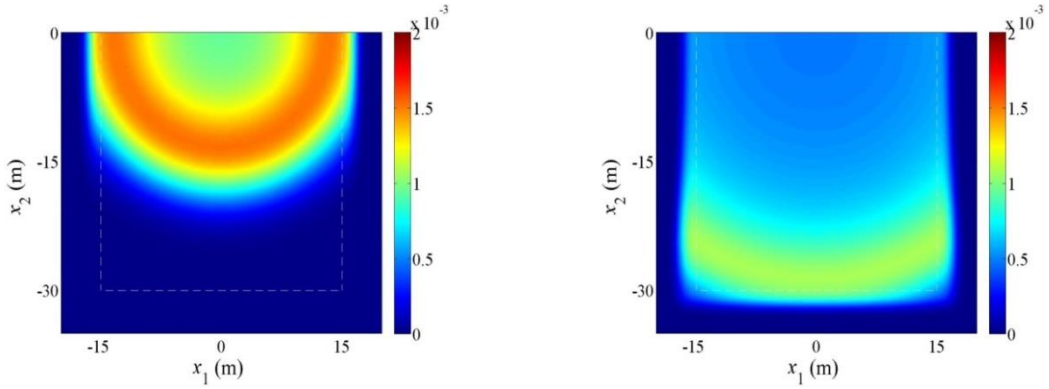

(a) u at t=100 s (b) u at t=1.50 s

Fig. 8 Contour plots of displacements generated by a Gaussian pulse load $p(t)$

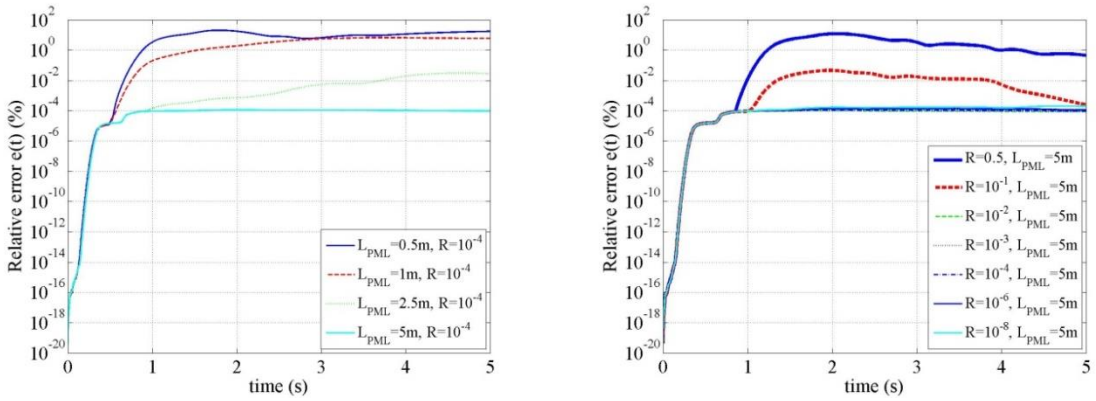

(a) Relative error for various L_{PML} (b) Relative error for various $|R|$

Fig. 9 Variation of the relative error $e(t)$ for various values of L_{PML} and $|R|$

where excellent agreement is observed. Fig. 7(b) displays the relative error $e(t)$, which is below 0.00012% at all times. Fig. 8 depicts fringe plots of the displacements taken at two distinct times. The figures show no reflections propagating back to the regular domain from either the side or bottom-PML zones.

Finally, the effect of PML parameters on the quality of solutions was investigated. For this purpose, different values of L_{PML} and $|R|$ were tested. Fig. 9(a) shows the relative error for various values of L_{PML} from 0.5m (one element) to 5m (10 elements). The relative error began to diverge at 0.5 s when reflections bounce back to the regular domain. A thicker PML results in stronger attenuation which causes smaller overall error. Next, the PML size was fixed, and the relative error was compared for various values of $|R|$ from 0.5 to 10^{-8}. According to Fig. 9(b), all cases showed the same relative error before 0.85 s. The relative error began to diverge for each of the cases beyond 0.85 s, but the graph was similar for the cases of $|R|$ less than 10^{-1}. For $|R|$ greater than 10^{-2}, the fixed exterior PML boundaries reflected higher amplitude waves back to the regular domain. Increasing the size of the PML may allow use of higher $|R|$ values but increases computational cost in the simulations. Values of $|R|$ less than 10^{-4} increase the

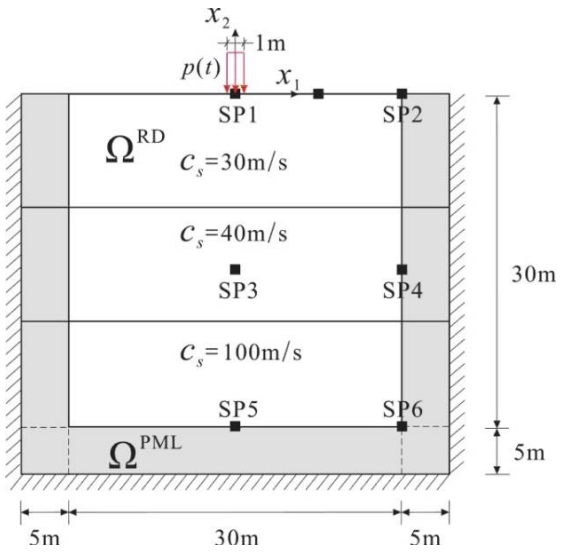

Fig. 10 A heterogeneous PML-truncated layered domain

relative error slightly because they reduce the absorptive capacity of the PML region. However, the magnitudes of the errors are acceptable for these time simulations.

5.2 Heterogeneous domain

To demonstrate the performance of the PML in heterogeneous media, layered and smoothly-varying shear wave velocity profiles were considered. For both cases, the loading conditions were the same as in the previous example (shown in Fig. 4).

5.2.1 Layered profile

Fig. 10 shows a 30m×30m layered domain surrounded by 5m PML, where shear wave velocities are defined as:

$c_s = 30\ \mathrm{m/s}$, for $-10\mathrm{m} \le x_2 \le 0\mathrm{m}$

$c_s = 40\ \mathrm{m/s}$, for $-20\mathrm{m} \le x_2 < -10\mathrm{m}$

$c_s = 100\ \mathrm{m/s}$, for $x_2 < -20\mathrm{m}$

For the side PMLs, shear wave velocity is assumed constant and equal to the velocity at the interface. Therefore, the side PML becomes homogeneous along the width (x_1) direction. The shear wave velocity in the bottom PML was also equal to the velocity in the third layer $(c_s = 100\ \mathrm{m/s})$. The six monitoring stations SPi were located as in Fig. 10 to report the response histories.

In Fig. 11, displacements obtained using the PML-truncated and enlarged domains are compared at several sampling points. The responses matched well in all cases. Fig. 12 depicts the L^2 norm and relative error for the layered heterogeneous case. The L^2 norms matched well, and the relative error $e(t)$ did not exceed 0.0027%. Fig. 13 presents fringe plots of the displacement responses taken at t=0.90 s and t=1.15 s, where the presence of layers is observed to affect the propagation patterns. Again, there are no obvious reflections even near the corners.

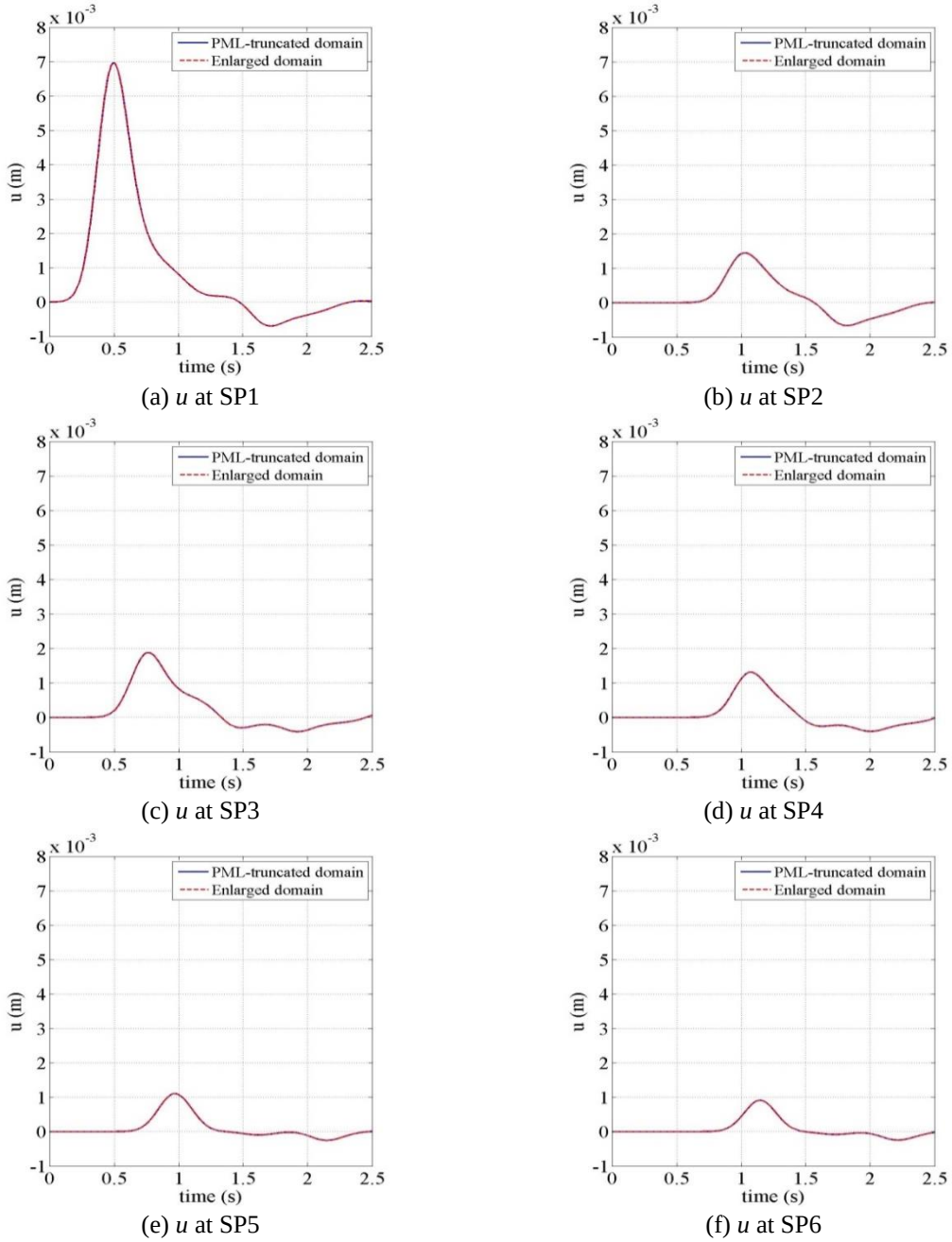

(a) *u* at SP1 (b) *u* at SP2

(c) *u* at SP3 (d) *u* at SP4

(e) *u* at SP5 (f) *u* at SP6

Fig. 11 Comparison of displacement time histories between enlarged and PML-truncated domain solutions at various sampling points; case with layered heterogeneous profile

5.2.2 Smoothly-varying heterogeneous profile

In the case of smoothly-varying shear wave velocity profile, the velocity profile in the 30 m×30 m domain is defined as

$$c_s = 30 + 30\exp\left[-\frac{(x_2+15)^2}{6}\right] \quad \text{(m/s)} \tag{65}$$

Fig. 14 compares the response of the regular domain with that of the enlarged domain. Both responses matched well at various sampling points. Fig. 15 shows the L^2 norm and relative error for the smooth velocity profile case. There is little difference for the L^2 norms between the PML-truncated and enlarged domains, and the maximum relative error is less than 0.00012%. Fig. 16(a) displays the wave motion passing through the high-velocity region of the profile, and the absorption of waves by the bottom PML is seen clearly in Fig. 16(b).

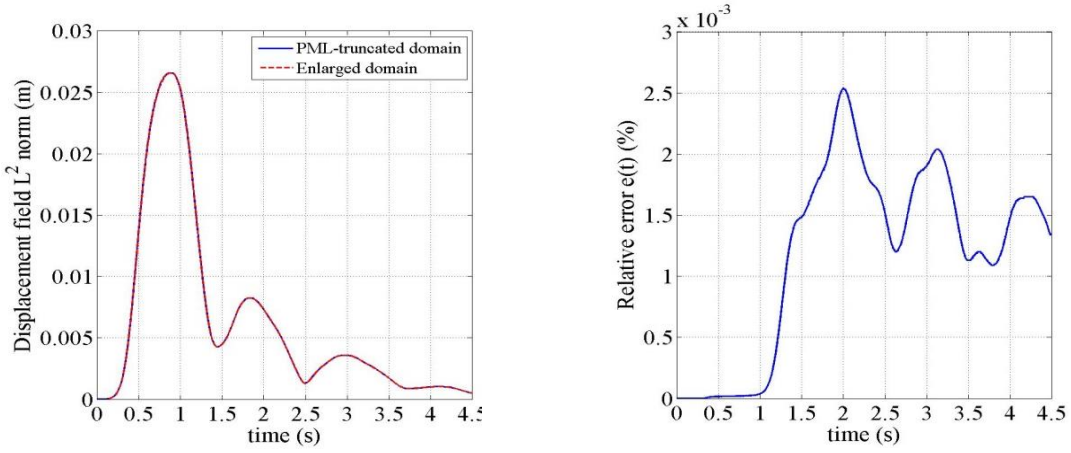

(a) Displacement field L^2 norm $D(t,\Omega^{RD})$ (b) Relative error $e(t)$

Fig. 12 Displacement field L^2 norm and relative error for the layered heterogeneous case

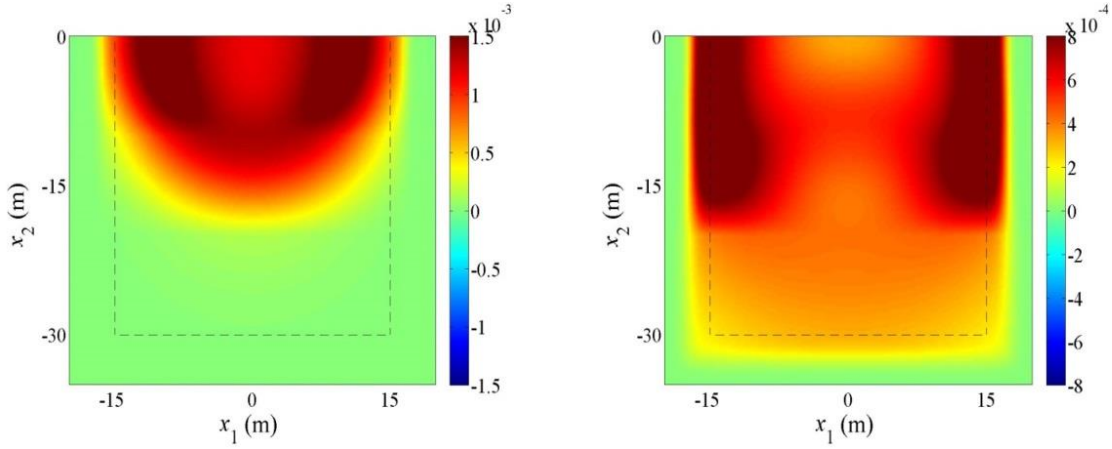

(a) u at t=0.90 s (b) u at t=1.15 s

Fig. 13 Contour plots of displacements for the layered heterogeneous case

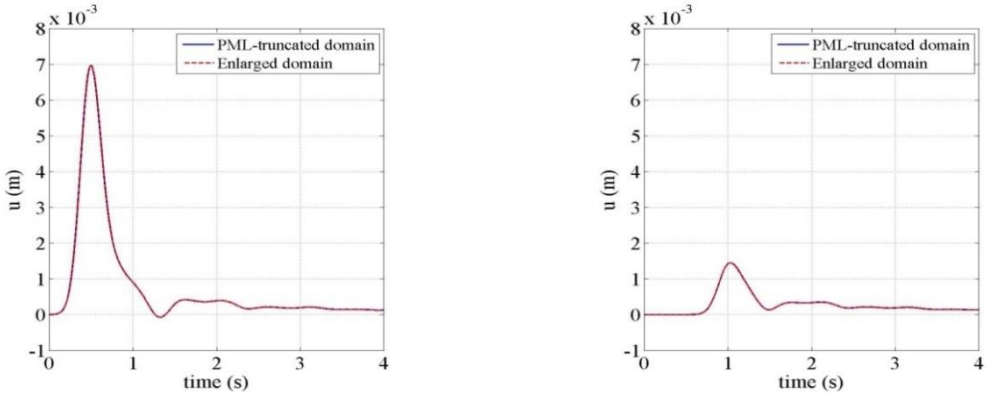

(a) *u* at SP1 (b) *u* at SP2

(c) *u* at SP3 (d) *u* at SP4

(e) *u* at SP5 (f) *u* at SP6

Fig. 14 Comparison of displacement time histories between enlarged and PML-truncated domain solutions at various sampling points; case with smoothly-varying heterogeneous profile

5.3 Computational cost

As mentioned before, fully-mixed PML formulation increases the unknowns in the PML-truncated domain as compared to a displacement-based formulation. In this Section, the number of

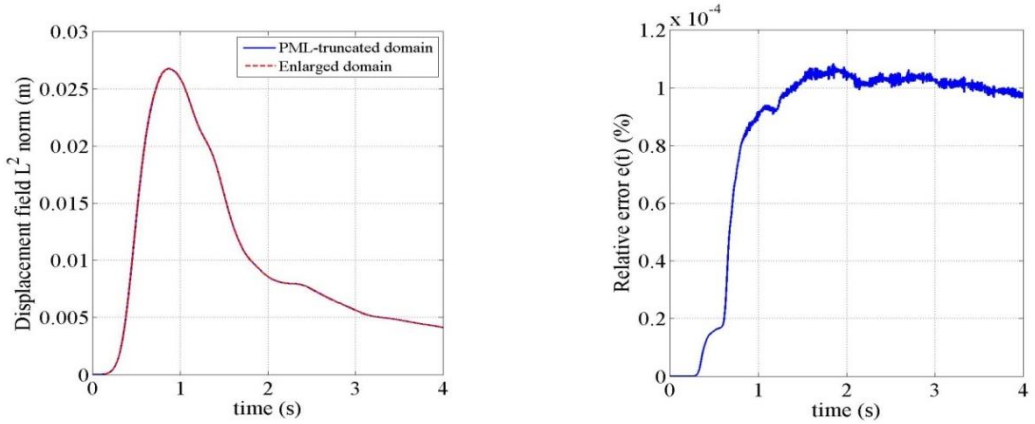

(a) Displacement field L^2 norm $D(t,\Omega^{RD})$ (b) Relative error $e(t)$

Fig. 15 Displacement field L^2 norm and relative error for the smooth velocity profile case

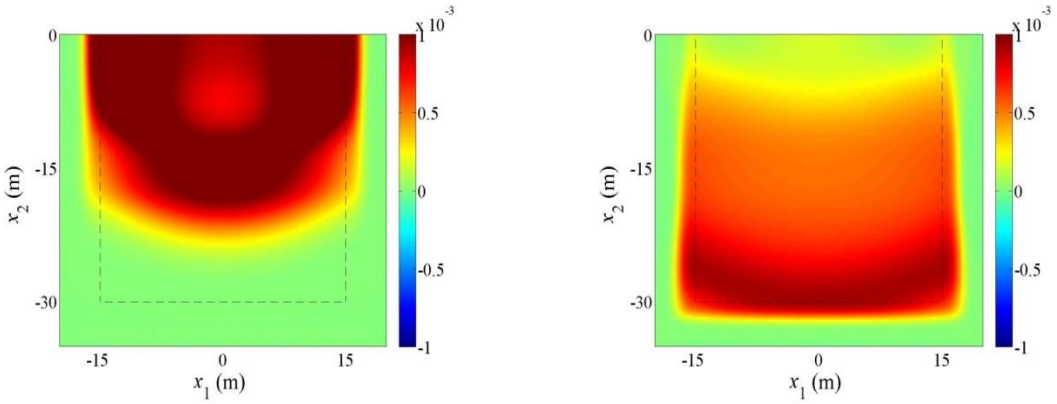

(a) u at t=1.00 s (b) u at t=1.45 s

Fig. 16 Contour plots of displacements for the smoothly-varying heterogeneous case

Table 1 Computational cost comparison between fully-mixed and hybrid formulations

Element length	0.5m	0.25m	Generic
# of nodes	14533	57577	n
# of regular domain nodes	10680	42960	r
# of (interface+PML) nodes	3853	14617	$i+p$
# of unknowns of the fully-mixed method (FM)	43599	172731	$3r+3(i+p)$
# of unknowns of the hybrid method (H)	22239	86811	$r+3(i+p)$
Savings (%)	49.0	49.7	$\left(\frac{\mathrm{H}-\mathrm{FM}}{\mathrm{FM}}\right)\times 100$

unknowns is compared between fully-mixed and hybrid formulations, and the results are shown in Table 1 for two sizes of element lengths in a 2D domain (30m×30m regular domain and 3m PML layers at the sides and bottom). The results indicate that the hybrid formulation reduces the number of unknowns to about fifty percent of the unknowns in a fully-mixed formulation.

6. Conclusions

In this study, a new formulation was developed to simulate scalar wave propagation in a PML-truncated domain. This method is straightforward and no iterative process is needed to solve the equations. To obtain the response, a displacement-based and a mixed formulation were used in the regular domain and the PML region, respectively. In the semi-discrete form of the equations, the components are mostly like the semi-discrete form of displacement-based finite elements but include additional components related to stresses within the PML. Owing to the additional components, the matrices become asymmetric. This formulation is more economical than the fully-mixed formulation where the stress components are also considered as unknowns in the interior domain. It is important to note that the resulting equations are second-order in time, similar to the standard form of the interior problem. If the mixed formulation of the PML region were to be replaced by a displacement-only form, the temporal complexity of the continuous problem and the corresponding semi-discrete forms would have been increased.

No instability was observed during the simulations. Different values of PML parameters were also used and the results were compared. The magnitude of the reflection coefficient $|R|$ imposed at the fixed outer boundaries of the PML zone is of importance in the numerical simulation. At fine discretization, the numerical results indicate that $|R|$ should be in the range of 10^{-4} to 10^{-2}. The size of the PML was also investigated: increasing the PML size reduced the errors, and at least 10 percent of the length of the domain in each direction is proposed for the size of a PML. However, a very large PML can increase computational cost for simulations. For both homogeneous and heterogeneous domains, several comparison plots and error analyses were provided between the PML-truncated and enlarged domains which showed excellent agreement. Lastly, computational cost analysis showed that using the hybrid formulation can reduce the number of variables by nearly fifty percent of the number of variables in the fully-mixed formulation.

Acknowledgments

This work was supported by the Hongik University new faculty research support fund. This support is greatly acknowledged.

References

Basu, U. (2009), "Explicit finite element perfectly matched layer for transient three-dimensional elastic waves", *Int. J. Numer. Method. Eng.*, **77**, 151-176.

Basu, U. and Chopra, A.K. (2004), "Perfectly matched layers for transient elastodynamics of unbounded domains", , *Int. J. Numer. Method. Eng.*, **59**, 1039-1074.

Bécache, E., Joly, P. and Tsogka, C. (2002) "A new family of mixed finite elements for the linear elastodynamic problem", *SIAM J. Numer. Anal.*, **39**(6), 2109-2132.

Bérenger, J.P. (1994), "A perfectly matched layer for the absorption of electromagnetic waves", *J. Comput. Phys.*, **114**(2), 185-200.

Brezzi, F. and Bathe, K.J. (1990) "A discourse on the stability conditions for mixed finite element formulations", *Comput. Method. Appl. Mech. Eng.*, **82**, 27-57.

Chew, W.C. and Liu, Q.H. (1996), "Perfectly matched layers for elastodynamics: a new absorbing boundary

condition", *J. Comput. Acoust.*, **4**(4), 341-359.
Chew, W.C. and Weedon, W.H. (1994), "A 3D perfectly matched medium from modified Maxwell's equations with stretched coordinates", *Microw. Opt. Tech. Lett.*, **7**(13), 599-604.
Drossaert, F.H. and Giannopoulos, A. (2007), "Complex frequency shifted convolution PML for FDTD modelling of elastic waves", *Wave Motion*, **44**(7-8), 593-604.
Frasca, L.P., Hughes, T.J.R., Loula, A.F.D. and Miranda, I. (1988) "A new family of stable elements for nearly incompressible elasticity based on a mixed Petrov-Galerkin finite element formulation", *Numerische Mathematik*, **53**, 123-141.
Hastings, F.D., Schneider, J.B. and Broschat, S.L. (1996), "Application of the perfectly matched layer (PML) absorbing boundary condition to elastic wave propagation", *J. Acoust. Soc. Am.*, **100**(5), 3061-3069.
Kang, J.W. and Kallivokas, L.F. (2010), "Mixed unsplit-field perfectly-matched-layers for transient simulations of scalar waves in heterogeneous domains", *Comput. Geosci.*, **14**, 623-648.
Komatitsch, D. and Tromp, J (2003), "A perfectly matched layer absorbing boundary condition for the second-order seismic wave equation", *Geophys. J. Int.*, **154**, 146-153.
Madsen, S.S., Krenk, S. and Hededal, O. (2013), "Perfectly matched layer (PML) for transient wave propagation in a moving frame of reference", *Proceedings of the 4th ECCOMAS Thematic Conference on Computational Methods in Structural Dynamics and Earthquake Engineering (COMPDYN 2013)*, Kos Island, Greece, June.
Mahmoud, A. and Luo, Y (2009), "Application of a Perfectly Matched Layer Boundary Condition to Finite Element Modeling of Elastic Wave Scattering in Cracked Plates", *Adv. Theor. Appl. Mech.*, **2**(2), 75-92.
Mahmoud, A., Rattanawangcharoen, N., Luo, Y. and Wang, Q. (2010) "FE-PML modeling of 3D scattering of transient elastic waves in cracked plate with rectangular cross section", *Int. J. Struct. Stab. Dyn.*, **10**(5), 1123-1139.
Martin, R., Komatitsch, D. and Gedney, S.D. (2008) "A variational formulation of a stabilized unsplit convolutional perfectly matched layer for the isotropic or anisotropic seismic wave equation", *Comput. Model. Eng. Sci.*, **37**(3), 274-304.
Martin, R., Komatitsch, D., Gedney, S.D. and Bruthiaux, E. (2010) "A high-order time and space formulation of the unsplit perfectly matched layer for the seismic wave equation using auxiliary differential equations (ADE-PML)", *Comput. Model. Eng. Sci.*, **56**(1), 17-40.
Matzen, R. (2011), "An efficient finite element time-domain formulation for the elastic second-order wave equation: A non-split complex frequency shifted convolutional PML", *Int. J. Numer. Method. Eng.*, **88**(10), 951-973.
Sagiyama, K., Govindjee, S. and Persson, P.O. (2013), "An Efficient Time-Domain Perfectly Matched Layers Formulation for Elastodynamics on Spherical Domains", Report No. UCB/SEMM-2013/09, University of California at Berkeley, Berkeley, California, USA.
Teixeira, F.L. and Chew, W.C. (2000), "Complex space approach to perfectly matched layers: a review and some new developments", *Int. J. Numer. Model.*, **13**, 441-455.
Turkel, E. and Yefet, A. (1998) "Absorbing PML boundary layers for wave-like equations", *Appl. Numer. Math.*, **27**, 533-557.
Xu, B.Q., Tsang, H.H. and Lo, S.H. (2013), "3-D convolutional perfectly matched layer models for dynamic soil-structure interaction analysis in the finite element time-domain", *Proceedings of the 4th ECCOMAS Thematic Conference on Computational Methods in Structural Dynamics and Earthquake Engineering (COMPDYN 2013)*, Kos Island, Greece, June.